Heliyon 10 (2024) e37233

Contents lists available at ScienceDirect

Heliyon

journal homepage: www.cell.com/heliyon

Research article

Single-cell RNA sequencing reveals intratumoral heterogeneity and multicellular community in primary hepatocellular carcinoma underlying microvascular invasion

Zhuoya Sun [a,2], Biao Gao [b,c,2], Lai Song [d], Biying Wang [e], Junfeng Li [b], Hao Jiang [b], Xuerui Li [b,c], Yang Yu [e], Zishan Zhou [e], Zizhong Yang [b,c], Xiaohui Sun [a], Tianyu Jiao [b], Xiao Zhao [a,1,**], Shichun Lu [b,1,***], Shunchang Jiao [a,1,*]

[a] *Department of Clinical Oncology, Chinese PLA General Hospital & Medical School of Chinese PLA, Beijing, China*
[b] *Department of Hepatobiliary Surgery, Chinese PLA General Hospital & Medical School of Chinese PLA, Beijing, China*
[c] *Nankai University, Tianjin, China*
[d] *Beijing DCTY Bioinformatics Technology Co., Ltd, Beijing, China*
[e] *Beijing DCTY Biotech Co.,Ltd, Beijing, China*

ARTICLE INFO

Keywords:
Hepatocellular carcinoma
Single-cell RNA sequencing
Microvascular invasion
SPP1$^+$ macrophages
Proliferative CD4$^+$ T cell population
Immunotherapy

ABSTRACT

Background: Microvascular invasion (MVI) is associated with an unfavorable prognosis and early recurrence of hepatocellular carcinoma (HCC), which is the crucial pathological hallmark of immunotherapy. While microvascular invasion (MVI) in hepatocellular carcinoma (HCC) currently lacks a detailed single-cell analysis of the tumor microenvironment (TME), it holds significant promise for immunotherapy using immune checkpoint inhibitors (ICI).
Methods: We performed single-cell RNA sequencing (scRNA-seq) on 3 MVI positive (MVIP) and 14 MVI-negative (MVIN) tumor tissues, as well as their paired adjacent non-tumoral tissues.
Results: We identified SPP1$^+$ macrophages and CD4$^+$ proliferative T cells as intertumoral populations critical for the formation of cold tumors and immunosuppressive environments in MVI-positive patients and verified their prognostic value in correlation with MVIP HCC patients. Additionally, we identified SPP1$^+$ dominated interactions between SPP1$^+$ macrophages and the immunosuppressive T population as contributors to MVI destruction and tumorigenesis.
Conclusions: We provide a comprehensive single-cell atlas of HCC patients with MVI, shedding light on the immunosuppressive ecosystem and upregulated signaling associated with MVI. These findings demonstrate that intercellular mechanisms drive MVI and provide a potential immunotherapeutic target for HCC patients with HCC and underlying MVI.

* Corresponding author. Department of Clinical Oncology, The Fifth Medical Centre, Chinese PLA General Hospital, Beijing, 100071, China.
** Corresponding author. Department of Clinical Oncology, The Fifth Medical Centre, Chinese PLA General Hospital, Beijing, 100071, China.
*** Corresponding author. Department of Hepatobiliary Surgery, The First Medical Centre, Chinese PLA General Hospital, Beijing, 100853, China.
E-mail addresses: dr.zx@163.com (X. Zhao), lusc_301@163.com (S. Lu), jiaosc@vip.sina.com (S. Jiao).
[1] Prof. Jiao is the lead corresponding author, and Prof. Lu and Prof. Zhao are co-corresponding authors.
[2] Dr. Sun and Dr. Gao are co-first authors.

https://doi.org/10.1016/j.heliyon.2024.e37233
Received 18 April 2024; Received in revised form 5 July 2024; Accepted 29 August 2024
Available online 31 August 2024

Key Findings

1. We identified diverse T cell subsets with detailed profiles of $CD4^+$ and $CD8^+$ populations, highlighting their proliferative and exhausted states, particularly in MVIP tissues.
2. We performed extensive characterization of macrophage subtypes, which revealed the predominant presence of immunosuppressive M2-like macrophages in MVIP tissues that are associated with enhanced tumor progression and poor prognosis.
3. We elucidated critical intercellular interactions and signaling pathways, particularly those involving SPP1-CD44 and SPP1-IGTA4/ITGB1, which contribute to the immunosuppressive TME.

Implications

1. We identified novel cellular targets and pathways for potential therapeutic interventions, particularly for enhancing the efficacy of immune checkpoint inhibitors.
2. We gave insights into the cellular composition and functional state of immune cells in MVIP HCC that provides a foundation for personalized and effective treatment strategies.

1. Introduction

Hepatocellular carcinoma (HCC) represents a significant health burden in China and is one of the leading causes of cancer-related fatalities in both genders [1]. Current therapeutic strategies, including surgical resection, liver transplantation, and tumor ablation, have undergone substantial advancements through innovations in laparoscopic techniques and living donor transplantations [2]. Despite these advancements, the application of immunotherapy in HCC treatment has introduced transformative outcomes; however, its effectiveness in individuals with considerable liver dysfunction necessitates further research to enhance patient stratification and treatment efficacy [3].

Among the numerous risk factors contributing to HCC recurrence, microvascular invasion (MVI), defined as the presence of tumor cells within the portal vein, hepatic vein, or large capsular vessel, stands out because of its prognostic significance. A remarkable fraction of MVI caused by hepatitis B virus (HBV) infection [4,5]. This phenomenon, which can be identified solely by histopathological examination, plays a pivotal role in predicting HCC recurrence and patient prognosis after surgery or immunotherapy [6,7]. Despite the improved prognosis observed in MVI-positive (MVIP) patients with the use of the Vascular Endothelial Growth Factor A (VEGFA)-targeted inhibitor sorafenib in conjunction with surgical interventions [8], its potential as a therapeutic target in combination with immune checkpoint inhibitors remains unclear. Therefore, the intricate processes involving tumor-infiltrating lymphocytes (TIL) and the tumor microenvironment (TME) in vascular invasion underscore the critical need for an in-depth understanding of these mechanisms.

Tumorigenesis and response to immunotherapy in HCC are profoundly influenced by the interplay between TIL and the TME. This complex system hosts a myriad of immune cells, including regulatory T cells (Tregs), tissue-resident memory $CD8^+$ T cells, resident natural killer (NK) cells, and tumor-associated macrophages (TAM) [9]. However, the efficacy of TIL, particularly NK and cytotoxic T cells, in mounting early anti-tumor responses gradually diminishes due to Treg-mediated immune tolerance and $CD8^+$ cell exhaustion [2]. Tigh levels of Tregs and exhausted $CD8^+$ cells, characterized by inhibitory receptors, such as PD-1 and CTLA-4, correlate with T-cell dysfunction and adverse patient outcomes.

Single-cell RNA sequencing (scRNA-seq) has revolutionized our understanding of the tumor immune microenvironment (TIME) in virus-associated cancers such as HCC. By providing a granular view of the immune landscape, scRNA-seq reveals complex immune responses and cellular heterogeneity at a resolution unattainable using bulk sequencing techniques [10]. This approach identified key leukocyte populations and anti-tumor responses, offering new avenues for the discovery of immunotherapy targets. Furthermore, scRNA-seq has shed light on the chromatin landscape of TIL, revealing the gene regulatory networks underlying their functional and dysfunctional states, and thus identifying novel targets for clustered regularly interspaced short palindromic repeats (CRISPR)-based gene editing [10]. However, limited research data is available on comprehensive characterization of the multicellular TME and the molecular features underlying MVI positive (MVIP) and MVI absent (MVIN) primary HCC at the single-cell level.

Confirming the positive correlation of MVI in HCC with an unfavorable prognosis using a previously published database, this study aimed to comprehensively describe the distribution and landscape of single cells through detailed scRNA-seq analysis of fresh tumor and adjacent non-tumor tissues obtained from 17 primary HCC patients with or without MVI. With further exploration of MVI, an immunosuppressive environment was revealed within MVIP HCC tumor tissues. This would provide new immunotherapeutic targets, leveraging the extensive data generated from scRNA-seq and clinical correlations to pioneer personalized and efficacious treatment modalities for HCC patients with MVI.

2. Methods

1 Patient samples collection

Seventeen patients diagnosed with primary HCC underwent surgical resection at the Chinese PLA General Hospital after providing written informed consents. Each patient provided paired samples of: tumor tissue (T) and adjacent tumor tissue (A), with the latter located 1–3 cm from the tumor margin, representing a transitional state from normal tissue to diseased tissue. Blood samples were collected from all patients before the surgery. Specimens were procured and used following the ethical standards set by the Ethics Committee of the Chinese PLA General Hospital, with patient confidentiality maintained through de-identified numerical identifiers.

2 Sample preparation of sequencing

Fresh tumors and adjacent tissues were cut into 1–3 mm^3 fragments and disaggregated using a Tumor Dissociation Kit Human and Gentle MACS Dissociator Machine to create a single-cell suspension in 10X PBS. After disintegration, the cell suspensions were collected and enumerated by observing them under 10× magnification in oil immersion.

3 Single-cell Sequencing

Single-cell transcriptomic information from HCC T and A samples was captured using the 10X Genomic Single-Cell Analysis System (Shanghai Biotechnology Corporation). Single-cell capture involves distributing a single-cell suspension across approximately 200,000 microwells, with beads carrying unique molecular identifiers (UMI) and cell barcodes loaded to near-saturation. After exposure to cell lysis buffer, polyadenylated RNA molecules were hybridized to the beads. The beads were pooled for reverse transcription, tagging each cDNA molecule at the 5′ end with a UMI and a cell label indicating its origin. Whole transcriptome libraries were prepared, sequenced, and processed using the 10X Genomics analysis pipeline.

4 Single-cell Data Processing

The sequencing data were demultiplexed and UMI matrices for T and A tissues were generated using the Cell Ranger pipeline (version 5.0.2) from 10X Genomics. Subsequent data processing was performed in R (v.4.3.2) using the Seurat package (v5). Quality control measures involved the exclusion of cells with aberrant gene counts, those indicative of doublets (>6000 genes), and those with insufficient gene expression (<200 genes). Cells exhibiting excessive mitochondrial gene UMI (>20 %) or an extreme UMI:gene ratio (outside the 1.3–10 range) were also discarded.

5 Cohort Data Integration, T cell and macrophage identification

Gene expression matrices were normalized and T cells were integrated using Seurat functions. Principal component analysis (PCA) was conducted using the first 30 principal components used for the clustering. Clusters with a significant average expression of T cell genes were extracted. Macrophages were identified using methods similar to those used for gene markers.

6 T Subset Classification, Clustering, and Marker Identification

T cells with detectable expression of either CD4 or CD8 were assigned to their respective clusters. The first 30 principal components (excluding these genes) from a randomly selected training set of 75 % of the cells were used to train a random forest classifier (RandomForest package in R) for $CD4^+$ and $CD8^+$ T cells. The remaining 25 % were used as the validation set. This classifier was then used to classify T cells with no detectable CD4 or CD8 expression (likely due to gene dropout) as either $CD4^+$ or $CD8^+$ T cells and then further clustered separately. After CD4/CD8 classification and separation, the top 3000 variable features were reselected for each group and the principal components were computed. The top 30 principal components were used to perform clustering using Seurat's FindNeighbours and FindClusters functions. The top marker genes for each cluster were identified using Seurat's FindAllMarkers function, and P values were determined using the Wilcoxon test.

7 Myeloid Subset Classification, Clustering, and Marker Identification

For the selected myeloid cells, 3000 variable features were chosen for each population, and principal component analysis was performed. Clustering was conducted using the first 30 principal components using Seurat FindNeighbors and FindClusters functions. The FindAllMarkers function in Seurat was used to identify the top marker genes for each cluster, and P values were determined using the Wilcoxon test.

8 Odds Ratio (OR) Distribution Analysis

The distribution was analyzed to calculate the OR for specific cell types and groupings using the Fisher's exact test. P values were corrected for multiple testing using the Benjamini-Hochberg procedure. This step controls the false discovery rate, adjusting the

Pvalues to account for the many statistical tests being performed. In this analysis, the "test_function.R" and "draw_analysis.R" were applied according to the previous research by Zhang Zemin [11].

9 Pseudo-time Trajectory Analysis

Pseudo-time analysis was performed on cells in the CD4, CD8 and myeloid populations separately using Monocle 3. Expression data were UMAP embedded using the Monocle function "reduce_dimension" with default parameters. $CD4^+$ T, $CD8^+$ T and myeloid population trajectories were rooted in the clusters CD4-CCR7, CD8-CXCR4 and Mono-CX3CR1, respectively.

10 Differential expression analysis and gene set enrichment analysis

Differential expression analysis comparing cells from treatment exposure or response groups was performed using the FindAllMarkers function with the parameter "min.pct = 0.25, thresh.use = 0.25". Following the analysis, genes with avg_log2 over 1 and p_val <0.05 were extracted from each group.

To assign pathway activity estimates to individual cells, GSVA was applied using the standard settings available on the Metascape website (https://metascape.org/gp/index.html#/main/step1).

11 Gene module enrichment analysis

To assess the cytotoxic and exhausted T cell functions, we computed the cytotoxic and exhausted scores for each cell type using the AddModuleScore function in Seurat. This was accomplished using canonical cytotoxic markers (GZMA, GZMB, GZMK, GNLY, IFNG, PRF1, and NKG7) for cytotoxicity and exhausted markers (LAG3, TIGIT, PDCD1, HAVCR2, CTLA4, LAYN, and ENTPD2) for exhaustion. The mean value of the module scores for a cell cluster (comprising more than ten cells) from an individual sample was calculated to represent the signature level.

For macrophages, the M0 markers (ACP5, BHLHE41, C5AR1, CCDC102B, CCL22, CCL7, COL8A2, CSF1, CXCL3, CXCL5, CYP27A1, DCSTAMP, GPC4, HK3, IGSF6, MARCO, MMP9, NCF2, PLA2G7, PPBP, QPCT, SLAMF8, SLC12A8, TNFSF14, VNN1), and M2 markers (ACHE, ADAMDEC1, APOBEC3A, APOL3, APOL6, AQP9, ARRB1, CCL19, CCL5, CCL8, CCR7, CD38, CD40, CHI3L1, CLIC2, CXCL10, CXCL11, CXCL13, CXCL9, CYP27B1, DHX58, EBI3, GGT5, HESX1, IDO1, IFI44L, IL2RA, KYNU, LAG3, LAMP3, LILRB2, NOD2, PLA1A, PTGIR, RASSF4, RSAD2, SIGLEC1, SLAMF1, SLC15A3, SLC2A6, SOCS1, TLR7, TLR8, TNFAIP6, TNIP3, TRPM4), and M2 markers (ADAMDEC1, AIF1, ALOX15, CCL13, CCL14, CCL18, CCL23, CCL8, CD209, CD4, CD68, CFP, CHI3L1, CLEC10A, CLEC4A, CLIC2, CRYBB1, EBI3, FAM198B, FES, FRMD4A, FZD2, GGT5, HRH1, HTR2B, MS4A6A, NME8, NPL, P2RY13, PDCD1LG2, RENBP, SIGLEC1, SLC15A3, TLR8, TREM2, WNT5B), were used for scoring.

The average module score for a cell cluster (comprising more than 10 cells) from an individual sample was calculated to determine the levels of these biomarkers.

12 TCGA analysis

HCC from The Cancer Genome Atlas (TCGA) database were performed using GSVA (1.50.0). The functions of "survival" and "survminer" were used to explore the correlation between the expression of genes of interest and overall survival. Patients were divided into high- and low-signature groups and hazard ratios (HR) were calculated.

13 Receptor-ligand communication between cell types

CellChat (1.6.1) was used to investigate intercellular interactions within the TME. "CellChatDB.human' was used as the receptor-ligand database. To evaluate the regulatory network ofMacro-SPP1, Treg, Tex, and CD4-MKI67 cells, Macro-SPP1 was considered as the presenting cell to check the functions of Macro-SPP1.

14 Immunohistochemistry (IHC)

Paraffin-embedded tissue sections from HCC patients were subjected to immunohistochemistry (IHC) using anti-KI67, anti-CD4, anti-SPP1, and CD163 antibodies. Ten fields were randomly selected for analysis and independently evaluated by two pathologists.

15 Flow Cytometry

$CD45^+$ cells were isolated using magnetic beads (Miltenyi Biotec) and characterized using flow cytometry. After incubation with an antibody cocktail, the cells were washed and analyzed using a flow cytometer (NL1006). Data analysis was conducted using FlowJo V10.8 software.

3. Results

1 Single cell transcriptome data generation and curation

To delineate the clinical and pathological features of MVIP HCC, a thorough analysis of The TCGA and a published HCC database [12] was conducted, which revealed a significant correlation between the presence of MVI and malignant characteristics in patients with HCC. Notably, MVIP patients displayed progressed Barcelona Clinic Liver Cancer (BCLC) state in The Cancer Genome Atlas (TCGA) database, elevated α-fetoprotein (AFP) levels and advanced Tumor, Node, Metastasis (TNM) stage in the published HCC database [12] (Fig. 1A–C), highlighting a strong association between MVI positivity and increased tumor aggressiveness. However, the underlying mechanism requires further investigation.

For a comprehensive investigation aimed at elucidating the heterogeneity of TIL within the TME of primary HCC underlying MVI, we used scRNA-seq to analyze TIL in tumor and adjacent non-tumoral tissues from 3 MVIP and 14 MVIN HCC patients without any previous treatment (Fig. 1D), with detailed clinical information (Additional_file1). Following data quality control and filtration, 333898 TIL cells were obtained, including 21164 cells from MVIP tumor tissues, 141291 cells from MVIN tumors, and 165052 cells from adjacent samples (Supplementary Fig. 1A). Sample-specific batch effects were limited, as evidenced by even mixing as shown by uniform manifold approximation and projection (UMAP; Supplementary Figs. 1B and C).

Eight major cell types were identified according to the expression of the corresponding canonical marker genes, including T cells (CD3E), Myeloid cells (LYZ), B cells (CD79A), natural killer (NK) cells (KLRD1), epithelial cells (TF), endothelial cells (PECAM1), proliferative cells (MKI67), interstitial cells (TAGLN) (UMAP, Fig. 1E, F and Supplementary Fig. Additional_file2). To further validate the existence of these TIL, flow cytometry was performed in all patients, and T cells ($CD3^+$), B cells ($CD19^+$), NK cells ($CD56^+$) and monocytes ($CD14^+$) within the myeloid population were verified in tumor and adjacent non-tumor samples (Supplementary Fig. 1E).

As for the significant heterogenic distribution across tissues and MVI group (Supplementary Figs. 1F and G), the fraction of each cell type was calculated and OR analysis was applied. T and myeloid cells contributed to the largest compositions, whereas myeloid cells significantly increased in tumor tissues, and T and B populations displayed the opposite phenomenon (Fig. 1G). Epithelial cells were strongly distributed in the tumor and MVIP groups, whereas T cells appeared to be adjacent and MVIN-enriched (Fig. 1G and H). Interestingly, this heterogeneity was dominantly observed in tumor and adjacent tissues of patients with MVIP, but not in those with MVIN(Fig. 1H). Regarding the infiltration process of immune cells, T, B, and NK cells were the most enriched tumor cells in the MVIP group, but myeloid and proliferative cells displayed the opposite performance.

Overall, this infiltration heterogeneity implies immune-infiltrating restriction, especially for cytotoxic T and B cells, and distribution to the formation of cold tumors. This corresponds to an unfavorable prognosis for patients with MVIP-HCC. In contrast, T cells and myeloid cells, with various well-known and complex functions in the TME, display the opposite distribution. Therefore, these two populations were further explored in subsequent analyses.

2 Immunosuppressive T cells evaluated in MVIP tumor tissues

Our analysis identified 168,763 $CD3^+$ T cells that were further stratified into several subsets. By employing robust clustering techniques, we identified 18 unique T cell populations, thereby illustrating the extensive heterogeneity of cellular phenotypes present within the TME (UMAP, Fig. 2A, and Additional_file2). Our study cohort included seven $CD4^+$ tumor-infiltrating lymphocyte (TIL) states, 13 $CD8^+$ TIL states, and two atypical T-cell aggregates, namely, CD4/CD8 double-positive (DPT) and CD4/CD8 double-negative (DNT) clusters (Supplementary Fig. 1H). Additionally, our analysis identified two types of innate-like lymphocytes, two mucosal-associated invariant T (MAIT) states, and a pair of natural killer T (NKT) cell clusters (Supplementary Fig. 1I).

The T cell landscape was predominantly defined by αβ T-cell phenotypes, although we observed particular subsets that suggest a potentially specialized function for γδ T cells, especially within two NKT cell subsets, as inferred from TRDC gene expression (Supplementary Fig. 1J). Furthermore, we identified transcriptionally unique T-cell states, especially those expressing MKI67 (encompassing both CD4-MKI67 and CD8-MKI67 subsets), which demonstrated marked proliferative activity, as evidenced by the upregulation of cell cycle-associated genes, including MKI67, TOP2A and SIVA1 (Fig. 2B). The existence of NKT, DPT, and DNT populations was further corroborated by flow cytometric analysis of both tumor and adjacent non-tumorous tissues (Supplementary Fig. 1K). The single-cell dataset we compiled not only emphasizes the diverse spectrum of TIL populations but also elucidates the complex synergy between adaptive and innate-like immune responses that contribute to the immunological milieu of hepatocellular carcinoma.

The T cell population also showed significant differences across tissues and the MVI groups (Supplementary Fig. 2A); therefore, we further compared the distribution of T cells between tumor tissues and adjacent tissues in patients with MVIP and MVIN. We found that proliferative $CD4^+$ T cells were significantly enriched in MVIP tumor tissues, whereas naïve $CD4^+$ T cells and exhausted $CD8^+$ T cells showed the opposite trend ($P < 0.05$, Fig. 2C).

$CD4^+$ and $CD8^+$ tissue-resident memory T cells (TRM) expressing high levels of functional factors such as GZMB and GZMK were also highly expressed in MVIP tumor tissues. Furthermore, cytotoxicity scoring of T cells in tumor tissues revealed a significant increase in the cytotoxic function of CD4, CD8, and NKT cells in MVIP tumor tissues, implying their activation in MVIP tumor (MVIPT) tissues (Fig. 2D). We also conducted exhaustion scoring for regulatory $CD4^+$ T cells (Tregs, CD4-FOXP3, and CD4-FOXP3/TNFRSF9) and exhausted T cells (Tex, CD8-PDCD1/GZMK, and CD8-PDCD1/CXCL13) and found a significant decrease in the exhaustion score of Tex cells in MVIN tumor tissues, whereas the exhaustion score of Tregs was higher in MVIP tumor tissues (Fig. 2E). To this end, we performed paired t-tests on Tregs in MVIP, revealing significant infiltration of CD4-FOXP3/TNFRSF9 ($TNFRSF9^+$ Treg) cells in the tumor tissues of patients with MVIP, which was not observed in patients with MVIN (Fig. 2F).

Subsequent analyses will involve a pseudo-temporal analysis integrated with tissue distribution to elucidate the intricate relationship between cell differentiation and infiltration. Notably, the CD8-TOX cluster was identified as a patient- and origin-specific entity, confined solely to the adjacent tissue of 12 patients (Supplementary Fig. 2B), thus necessitating its exclusion from the

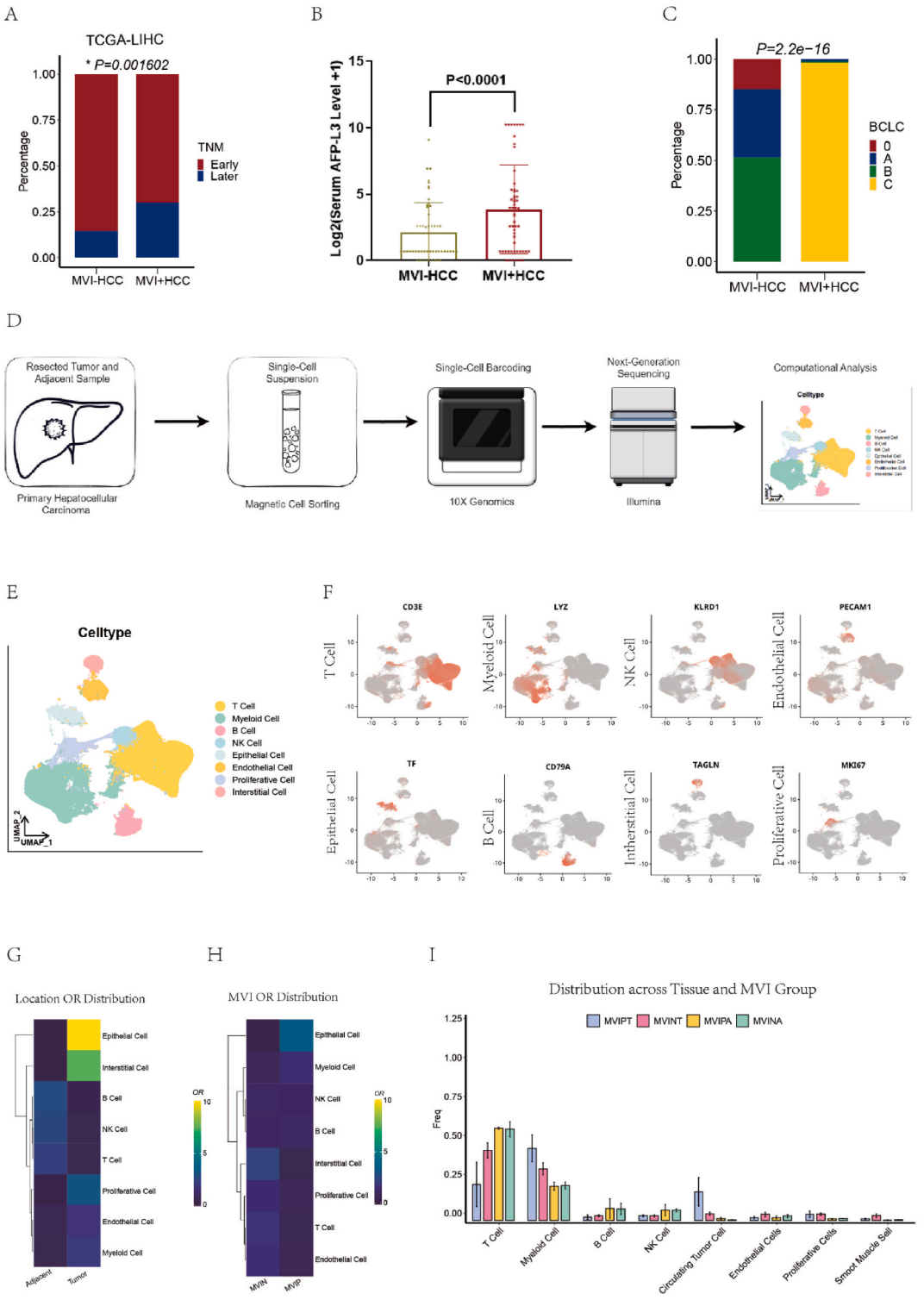

(caption on next page)

Fig. 1. Clinical analysis of MVIP HCC; Clustering, differential gene expression and composition landscape of primary HCC TIL. (A) Bar chart comparing the TNM stage in patients with HCC, grouped by the MVI presence (MVI+) and MVI absent (MVI-). The P-value indicates a significant difference between the two groups. (B) Box plot illustrates the serum AFP-L3% levels (log2-transformed) in patients with HCC, grouped by MVI+ and MVI-. The P-value indicates a significant difference between the two groups. (C) Stacked bar chart comparing the distribution of BCLC) stage patients with HCC, grouped by MVI+ and MVI-. The P-value indicates a significant difference between the two groups. (D) Experimental workflow showing the collection and procession of fresh HCC tissue and paired adjacent non-tumoral tissues for scRNA-seq. (E) Uniform manifold approximation and projection (UMAP) visualization showing the major cell types. Colors indicate different cell types. (F) UMAP visualization showing the expression of canonical cell type marker genes. Heatmap showing the ORs of metaclusters occurring in each tissue (G), and MVI groups (H). OR >1.5 indicates that metacluster is preferred to distribution in the corresponding tissue or group. (I) Bar graph compares the proportion of each cell types between microvascular invasion positive (MVIP, purple) and microvascular invasion negative (blue) and statistically significant differences between the two conditions are indicated above the bars.

pseudo-temporal analysis owing to its unique occurrence in a singular sample. Acknowledging the divergent developmental trajectories of $CD4^+$ and $CD8^+$ T cells after thymic selection, distinct trajectory analyses and pseudo-time descriptions were performed for each subset. Differentiation pathways of $CD8^+$ T cells are more complex than those of $CD4^+$ T cells. However, both subsets initiated differentiation with heightened expression of CCR7 in CD4-CCR7, CD8-CXCR4, and TRM populations, progressively transitioning through functional cell states before culminating in differentiation towards Tregs and Texs (Fig. 2G and I). Notably, TRM, which are characterized by their tissue-resident nature, do not participate in the circulatory pool of $CD4^+$ and $CD8^+$ cells. Intriguingly, upon integrating the differentiation trajectories of $CD4^+$ and $CD8^+$ cells with tissue infiltration dynamics, a striking alignment emerged between the infiltration process of $CD4^+$ cell populations from tissues adjacent to tumor tissues and their differentiation pathways, manifesting as a significant influx of terminal $TNFRSF9^+$ Tregs into the TME (Fig. 2G and H). Given the immunosuppressive properties of Tregs, which are pivotal in fostering tumor evasion and proliferation, their pronounced enrichment within the tumor tissues of MVI-positive patients underscores the propensity of MVI to engender an immunosuppressive milieu. In contrast, as $CD8^+$ cell populations differentiated into exhausted $PDCD1^+$ $CD8^+$ cells and exhibited a notable deficiency in tissue infiltration capabilities (Fig. 2I and J). With heightened expression of the immune checkpoint PDCD1, Tex cells have emerged as pivotal targets for anti-PD-1 immunotherapy. The absence of Tex cells in the MVIPT tissues explains the diminished therapeutic efficacy observed in these studies. Moreover, the analysis of proliferative markers, particularly MKI67, in $CD4^+$ T cells within MVIP tumors and gene set enrichment analysis (GSEA) underscored the shared proliferative pathways between CD4-MKI67 and CD8-MKI67 cells, while also revealing the signal overlaps of adaptive response to stimulus with Treg group (Supplementary Fig. 2C). The enrichment of the expression of MKI67 has been validated by immunohistochemical analysis (Fig. 3A). In TCGA database, genes related to CD4-MKI67 were overexpressed in MVIP tumor tissues, with survival analysis indicated a correlation with poor prognosis, underscoring the importance of these markers in understanding and treating MVI in cancer (Fig. 3B and C).

The distribution of T clusters implies the infiltrating district of TME in MVIP group, especially the $TNFRSF9^+$ Treg and $CD4^+$ proliferative T cells, which promotes the formation of "cold tumor". To some extent, this phenomenon explains poor prognosis and suboptimal immunotherapeutic efficacy.

3 Expansion of immunosuppressive macrophages in patients with MVI

The heightened proportion of myeloid cells in MVIP tissues warrants attention, as they are predominantly enriched within tumor tissues and exert an influence on tumor plasticity and progression. Within the TME, macrophages exhibited significant heterogeneity, comprising two monocyte groups (Mono-CX3CR1 and Mono-VEGFA) and five distinct macrophage subtypes (Macro-SPP1, Macro-CXCL10, Macro-C1QA, Macro-SELENOP, and Macro-CXCL9) (visualized via UMAP, Fig. 4A).

Specifically, Mono-VEGFA, characterized by reduced expression of typical monocyte markers but elevated expression of MHC-II molecules (HLA-DRA, HLA-DQA1, HLADPA1, and CD74), suggests a pre-macrophage state (Fig. 4B, C and Supplementary Fig. 2D). In contrast, Mono-CX3CR1 exhibited high expression of monocyte markers (VCAN, FCN1, S100A8, and S100A9) and low expression of the naive marker SELL, signifying a naive-like status (Fig. 4B and C). Notably, the expression of VEGFA by Mono-CX3CR1, indicative of an immunosuppressive and pro-angiogenic phenotype, demonstrated a pronounced preference for adjacent non-tumor tissues, as revealed by OR analysis (Fig. 4D).

In the macrophage domain, Macro-FABP4, identified as tissue-resident alveolar macrophages (AMs), expressed FABP4 and MACRO, indicating its residency (Fig. 4B and C). Other macrophages bear a resemblance to TAM, with Macro-SPP1 TAM expressing high levels of SPP1 and TNF alongside the immunosuppressive markers GPNMB and APOE. Conversely, Macro-CXCL9 macrophages exhibit proinflammatory characteristics through CXCL9 and CXCL10 expression, coupled with an elevated antigen presentation profile. The expression of CD274 (PD-L1) in Macro-C1QA highlights its critical role in anti-PD1 immunotherapy.

Macrophages are primarily classified into M0 (non-polarized or neutral), M1 (pro-inflammatory or anti-tumor), and M2 (anti-inflammatory and pro-tumor) subgroups, which aids in deciphering their functional dynamics [13]. This classification revealed that the Macro-FABP4 subset predominantly exhibited an M0-like phenotype, whereas Macro-CXCL9 displays significant M1 characteristic (Fig. 4E). Conversely, Macro-SPP1, Macro-C1QA, and macro-SELENOP distinctly expressed M2 signatures, whereas Macro-SPP1 showed notably low levels of M1 signatures.

In the context of MVI, unlike T cells, myeloid cells were substantially presenting patients with MVI and displayed significant heterogeneity (Supplementary Fig. 2E). Therefore, we examined the distribution and functions of myeloid cell subsets to gain further insights into the nuanced role of myeloid cells in HCC progression and underscore their potential impact on therapeutic resistance and

disease outcomes.

Our investigation revealed distinct enrichment patterns of macrophages across different MVI cohorts, notably highlighting a significant abundance of Macro-SPP1 within MVIP tumor tissues, while Macro-CXCL9 presenting an opposing trend (Fig. 4F). Moreover,

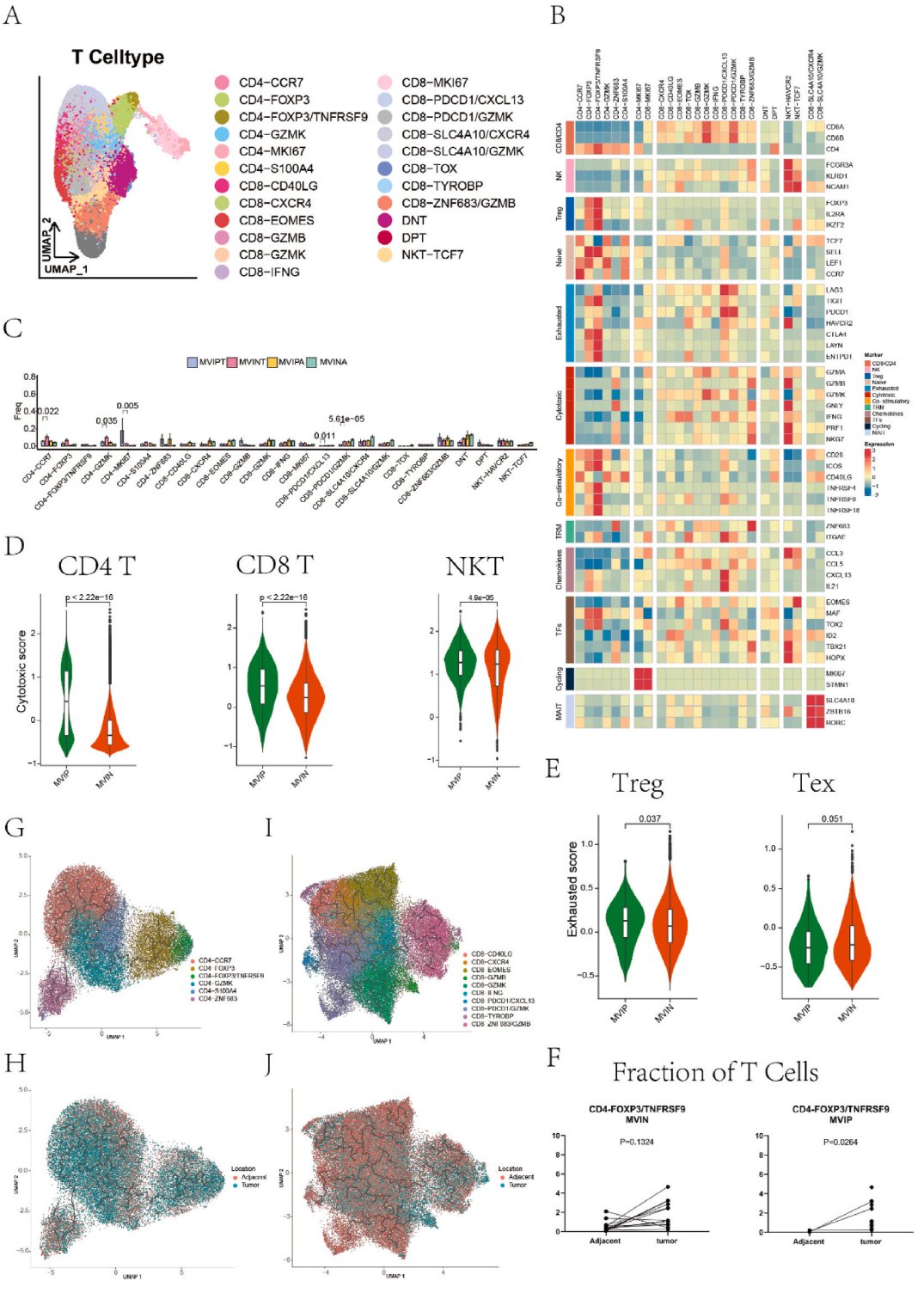

(caption on next page)

Fig. 2. T cell clustering, differential gene expression and pseudotime analysis of CD4/CD8 clusters. (A) UMAP visualization showing the expression of T cell type marker genes. (B) Heatmap of normalized expression of canonical T cell marker genes among clusters. TRM, tissue-resident memory; MAIT, mucosal associated innate T. (C) Multiple bar graphs comparing the fractions of various genes across MVIP tumor (MVIPT), MVIN tumor (MVINT), MVIP adjacent (MVIPA) and MVIN adjacent (MVINA). Statistically significant differences among these groups are indicated above the bars. (D) Violin plots of average cytotoxic signatures scores for $CD4^+$, $CD8^+$ and NKT clusters in MVIP (n = 3) and MVIN (n = 14) patients. One-sided *t*-test was used. (E) Violin plots of average exhausted signatures scores for Treg and exhausted T (Tex) clusters in MVIP (n = 3) and MVIN (n = 14) patients. One-sided *t*-test was used. (F) Comparison of CD4-FOXP3/TNFRSF9 state frequencies between matched tumor and adjacent samples in MVIN (left, n = 14) and MVIP (right, n = 3). $P < 0.05$ is displayed in MVIP patients and were generated using a paired Wilcoxon statistical test. Monocle 3 pseudotime trajectory inference analysis for (G) $CD4^+$ TIL. (I) $CD8^+$ TIL. Colors indicate different cell types. Monocle 3 pseudotime trajectory inference analysis for (H) $CD4^+$ TIL. (J) $CD8^+$ TIL. Colors indicate different tissues. (G) Gene Expression Trends with the pseudotime trajectory. The plots represent the expression levels of specific genes in $CD4^+$ TIL (left) and $CD8^+$ TIL (right). Colors indicate tissue distribution.

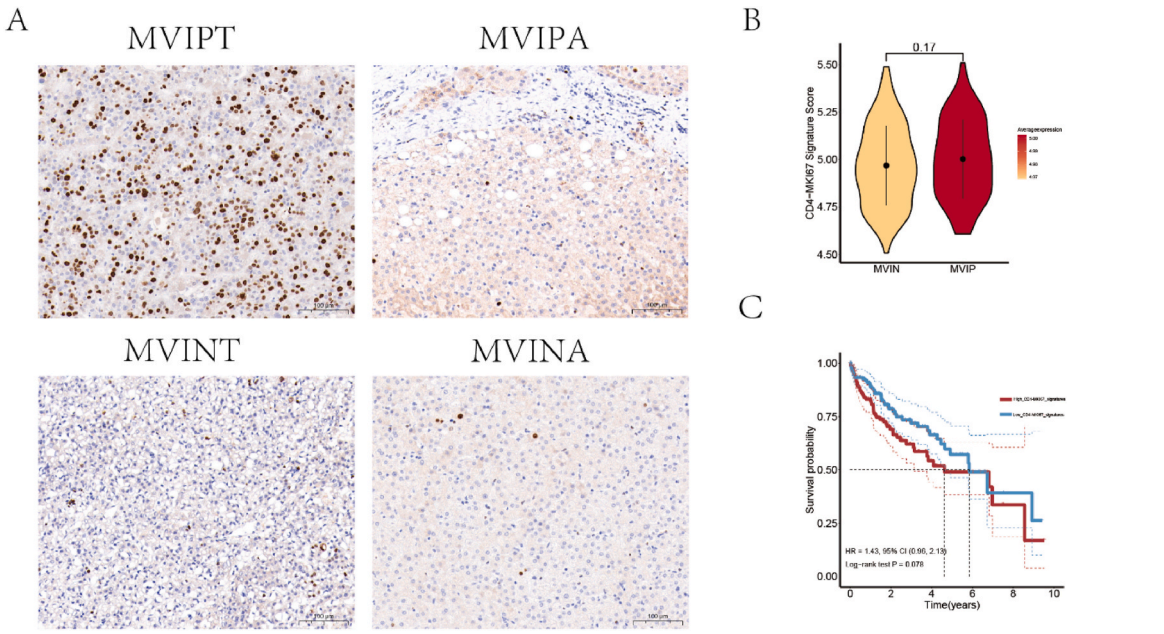

Fig. 3. Upregulation of the expression of KI67 in MVIPT (A) IHC staining image of KI67 in MVIPT (upper left), MVIPA (upper right), MVINT (down left) and MVINA (down left). (B) Violin plots of average CD4-MKI67 signatures scores for TCGA database in MVIP (n = 106) and MVIN (n = 205) patients. One-sided *t*-test was used. (C) Survival analysis between the groups with high and low CD4-MKI67 signatures. The hazard ratio (HR) and its confidence interval (CI) are provided, indicating the relative risk of an even.

our evaluation of macrophage polarization states in tumor tissues across diverse MVI statuses revealed the prevailing M2 polarization within the tumor tissues of MVI-positive patients (Fig. 4G). To deepen our understanding, we conducted GSEA for Macro-SPP1 and Macro-CXCL9, elucidating that Macro-SPP1 is primarily associated with angiogenesis and receptor tyrosine kinase signaling, whereas Macro-CXCL9 exhibits notable correlations with cytokine signaling within the immune system (Supplementary Fig. 2H). The notable enrichment of SPP1 in MVIP tumor tissues was further validated by IHC analysis (Fig. 5A). Additionally, validation from the TCGA database confirmed the upregulated expression of Macro-SPP1 signatures in MVIP patients, aligning with significantly decreased survival probabilities ($P = 0.0056$, Fig. 5B and C).

Pseudo-temporal inference applied to the myeloid cell population identified Mono-CX3CR1 as the starting point, with Macro-SPP1 positioned as an intermediate state, diverging into two developmental pathways (Fig. 6A). By integrating pseudo-temporal pathways with tissue distribution, we observed that the differentiation of monocytes into Macro-SPP1 cells aligns with their infiltration process (Fig. 6B), and the expression of SPP1 significantly increased during this infiltration process (Fig. 6C).

4. Macro-SPP1 may contribute to the immunosuppressive environment of HCC underlying MVI

Through cell chat analysis, we uncovered intricate intercellular interactions, particularly highlighting the significant engagement between Macro-SPP1 and CD4-MKI67 clusters with Tregs and exhausted T cells in MVIP samples (Fig. 6D). This finding delineates a complex network of signaling pathways, notably through SPP1-CD44 and SPP1-IGTA4/ITGB1, which likely facilitates the establishment of an immunosuppressive environment conducive to tumor progression and evasion of immune surveillance (Fig. 6E). Consistently, T cells showed significantly higher expression of CD44 and IGTA4/IGTB1 ($P < 0.001$, Fig. 6F).

The observed preferences and functional attributes of the macrophage subsets were validated using an external databases [14]. We

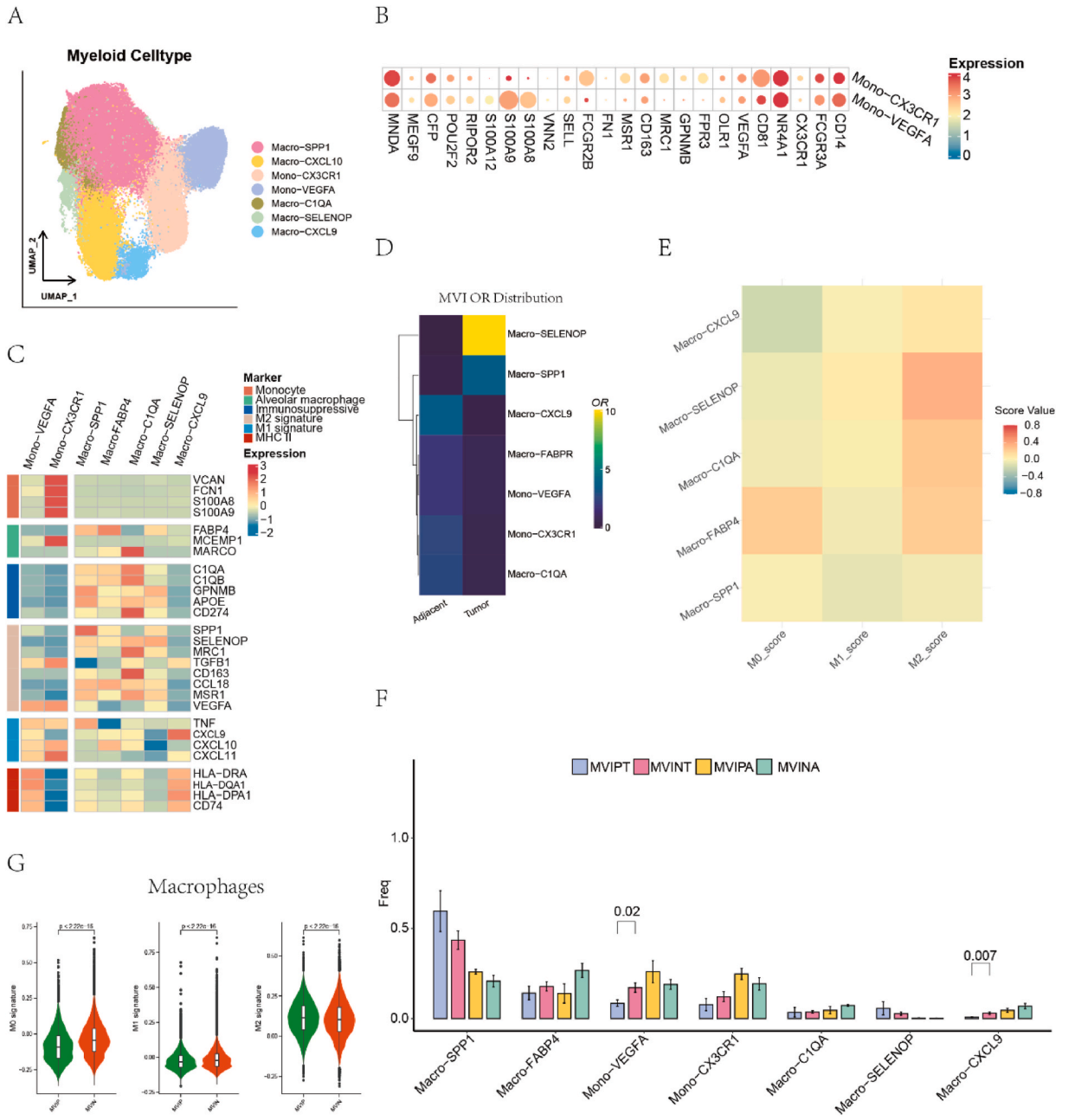

Fig. 4. Myeloid cell clustering, differential gene expression and pseudo-time analysis. (A) UMAP visualization showing the expression of myeloid cell type marker genes. (B) Heatmap of selected marker genes of defined monocyte clusters. (C) Heatmap of normalized expression of monocyte and macrophage canonical cell marker genes among clusters. (D) Heatmap showing the ORs of meta clusters occurring in each tissue. OR >1.5 indicates that meta cluster is preferred to distribution in the corresponding tissue or group. (E) Heatmap of module scores of M0, M1and M2 signatures among macrophages clusters. (F) Multiple bar graphs comparing the fractions of various genes across MVIPT, MVINT, MVIPA and MVINA. Statistically significant differences among these groups are indicated above the bars. (G) Violin plots of average M0, M1 and M2 signatures scores for macrophage clusters in MVIP (n = 3) and MVIN (n = 14) patients. One-sided *t*-test was used.

identified 3370 macrophages within 43082 cells; among them, 1739 SPP1^{+} macrophages showed a significant preference in MVIP tumor tissues (Fig. 6G and H, Supplementary Figs. 2I and J), and confirmed the association of high SPP1 expression with MVIP patients (Fig. 6I). This correlation, together with the verified increase in CD44 and IGTA4/ITGB1 signaling in MKI67^{+} tumor tissues, reinforces the pivotal role of these macrophages in shaping the TME and influencing HCC outcomes (Fig. 6J). These significant correlations between SPP1-CD44 and SPP1-ITGA4/ITGB1 signaling were also verified in TCGA-ICGC database, with $P < 0.001$ (Fig. 6K and L).

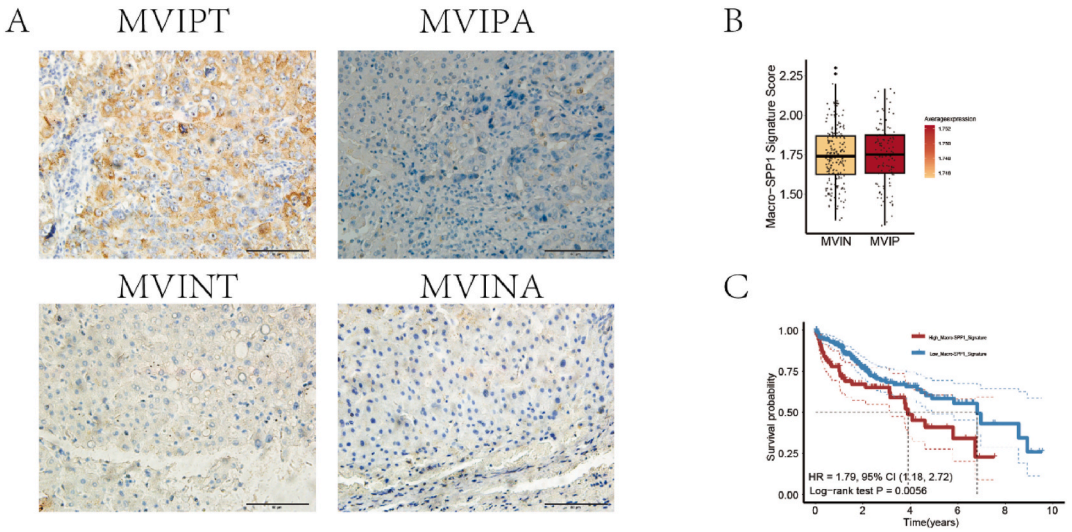

Fig. 5. Upregulation of Spp1+ macrophages in MVIPT (A) IHC staining image of SPP1 in MVIPT (upper left), MVIPA (upper right), MVINT (down left) and MVINA (down left). (B) Violin plots of average Macro-SPP1 signatures scores for TCGA database in MVIP (n = 106) and MVIN (n = 205) patients. One-sided *t*-test was used. (C) Survival analysis between the groups with high and low Macro-SPP1 signatures. And HR and its CI are also provided.

4. Discussion

Despite being a critical risk factor for early HCC recurrence and poor prognosis [15,16], little research has been conducted on MVI at the single-cell level. In this study, we meticulously delineated the heterogeneity within TIL populations in the context of primary HCC with MVI, revealing a complex landscape of T and myeloid cells characterized by distinct transcriptomic profiles. Using scRNA-seq combined with tissue-specific analysis, pseudo-temporal and cellular interaction analyses, and flow cytometry of paired tumors and adjacent tissues, we uncovered a comprehensive landscape of cellular heterogeneity and interactions in MVI-positive primary HCC. Notably, our study highlights the presence and role of specific T cell and macrophage populations, identifying the cellular communities within tumor tissues associated with MVI. To ensure the robustness of our findings, we used data from The TCGA and another external database for validation [14].

Although much attention has been focused on T cells in the TME of HCC and other solid tumors [9,11,17,18], our findings underscore the promotion of proliferative $CD4^+$ T cells within the TME by MVI, marking a shift towards an immunosuppressive TME characterized by an exhausted T cell signature in MVIP samples. The increase in the proliferative T cell population represents similar exhausted signatures and is characterized by a composition of immunosuppressive TME in MVIP samples [7]. In our study, $CD4^+$ proliferative T cells were specifically identified based on the fraction evaluation in MVIPT and poor survival probability with its signatures. With decreased cytotoxicity and enhanced proliferative abilities, the proliferative $CD4^+$ T cell cluster may compensate for its limited antitumor response [19]. Additionally, the enrichment of TRM, as indicated by ZNF683 and GZMB expression in MVIPT tissues, suggests a reactive mechanism and pro-inflammatory reactivity. The high expression levels of immune checkpoints such as PD-1, CTLA-4, and TIM-3 in these cells highlight their potential targets for immune checkpoint inhibitor (ICI) therapy in HCC with underlying MVI [20].

Furthermore, we delineated the role of macrophages in the TME. Recent studies, particularly those focusing on M2 macrophages, have shown their immunosuppressive and angiogenic effects, which are particularly pertinent in HCC [7,21,22]. MVI-burden HCC was found to have an increased infiltration of M2 macrophages and fewer T cells in tumors [23]. Consistently, we found increased infiltration of M2-like macrophages, characterized by significant SPP1 expression, in MVIP tumors, which correlated with lower survival probabilities. The cellular regulatory network between Macro-SPP1 and the proliferative $CD4^+$ T cell cluster, mediated by the SPP1-CD44 and SPP1-IGTA4/ITGB1 axes, was identified, highlighting the enhanced cellular interactions of Macro-SPP1 with Tregs and exhausted $CD8^+$ T cell groups. The upregulation of CD44 and IGTA4/ITGB1 associated with MVI was confirmed using an external validation dataset. Previous studies have positioned Macro-SPP1 as a pivotal mediator of tumorigenesis and the response to immunotherapy. These macrophages, through high SPP1 expression, can restrict TIL infiltration by stimulating extracellular matrix (ECM)-related genes in FAP^+ fibroblasts [24]. Meanwhile, the signatures of Macro-SPP1 were consistent with $APOE^+$ macrophages identified in a study on MVIP HCC, which contributed to aberrantly increased lipid metabolism and resistance to anti-PD-1 immunotherapy [22]. However, the cellular interactions between macrophages and the T cell population in MVIP HCC have rarely been discussed. Our findings predicted that Macro-SPP1 cells promote the proliferation of $CD4^+$ T cells via SPP1-CD44 and SPP1-IGTA4/ITGB1 interactions, and underscore the critical need for targeted interventions aimed at modulating the immunosuppressive activities of macrophages, offering new avenues for enhancing HCC treatment efficacy and improving patient prognoses.

Limited examination methods, diagnosis in the later stages of HCC [15,22], and immunosuppressive TME [7] contribute to the

reduced disease-free survival of patients with MVIP-HCC. Recently, a combination of ICI and stereotactic body radiation therapy (SBRT) was applied in MVIP-HCC [25],. However, a multicenter cohort study in China demonstrated the association of MVI with suboptimal immunotherapy response and poor prognosis of HCC [26]. This calls for a deeper understanding of the TME and discovery of new ICI targets. With the development of scRNA-seq, multiple types of TIL and their interactions within TME have been identified. Former study on MVIP HCC described a immunosuppressive network characterized by cycling T and Treg [7]. We further focused on the $CD4^+$ proliferative T population and revealed its intercellular communication with $SPP1^+$ macrophages according to SPP1-CD44 and SPP1-IGTA4/IGTB1 interactions. Furthermore, Wang et al. also found the oncogenic effects of SPP1- CD44 axis, a pathway through

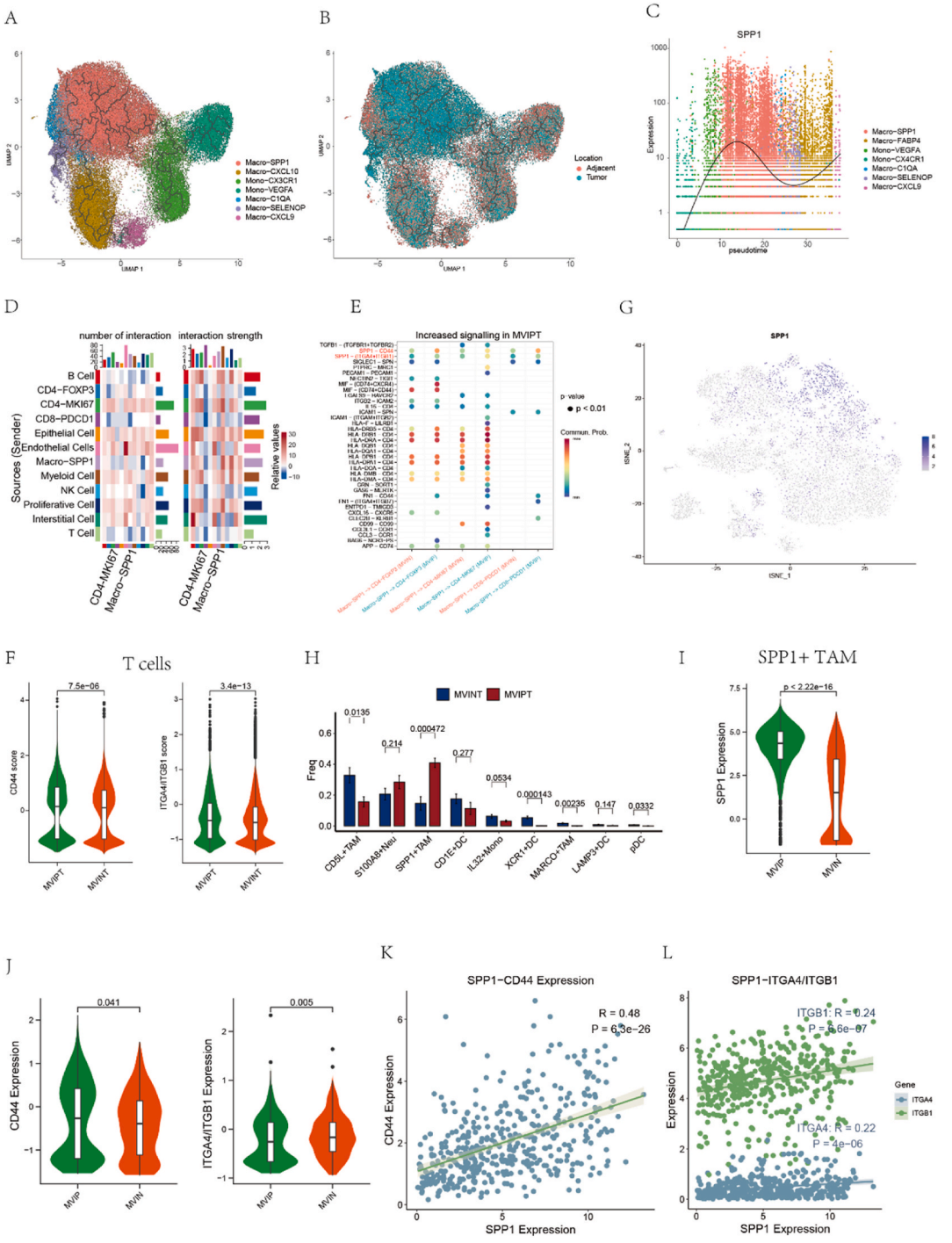

(caption on next page)

Fig. 6. Pseudo-temporal analysis of myeloid population; Differences in molecular signatures between MVIP and MVIN – HCC – derived cells and verification of external database. Monocle 3 pseudo-time trajectory inference analysis for monocyte and macrophage TIL. Colors indicate different cell types (A) and different tissues (B). (C) SPP1 Expression Trends with the pseudo-time trajectory. (D) Heatmap showing the number of interaction (left) and interaction strength (right) in MVIP HCC patients (E) Bubble plot showing the interaction from Macro-SPP1 to CD4-MKI67, and Tex subsets in MVIP and MVIN HCC. Statistically significant ligand-receptor pairs ($P < 0.05$) were selected. Colour represents different tissues and dot size indicates the interaction probability. (F) Violin plots of CD44, average of ITGA4/ITGB1 signatures scores for T clusters in MVIP ($n = 3$) and MVIN ($n = 14$) patients. One-sided *t*-test was used. (G) TSNE visualization showing the expression of SPP1+ TAM in MVIPT group. (H) Bar graph compares the proportion of each cell types between MVINT (blue) and MVIPT (red) and statistically significant differences between the two conditions are indicated above the bars. (I) Violin plots of SPP1 signature score for macrophage clusters in MVIP ($n = 3$) and MVIN ($n = 7$) patients. One-sided *t*-test was used. (J) Violin plots of CD44, average of ITGA4/ITGB1 signatures scores for T clusters in MVIP ($n = 3$) and MVIN ($n = 7$) patients. One-sided *t*-test was used. (K) Correlation of SPP1 expression with CD44 (left) with an R-value of 0.48 and a P-value of 6.3e-26; (L) Correlations of SPP1 expression with ITGA4/ITGB1 (right), which was indicated by R-values and P-values: ITGA4 ($R = 0.22$, $P = 4e\text{-}06$) and ITGB1 ($R = 0.24$, $P = 6.6e\text{-}07$).

which APOE$^+$ macrophages promote iCAFs differentiation [22]. These findings suggest the immunotherapeutic potential of the SPP1-CD44 axis.

However, some limitations of this study should be acknowledged. First, the three MVIP samples were small in number compared to those in the MVIN group, which may have influenced the statistical power and generalizability of our findings. Future studies with larger sample sizes are required to validate these findings. Second, owing to the recent enrollment of patients, it was not possible to validate the results using the clinical prognoses of existing patients. Therefore, we need to continue tracking the subsequent progress of the enrolled patients through follow-up. Lastly, while our study identified potential therapeutic targets and mechanisms for HCC with MVI, further research is required to translate these findings in clinical applications.

In conclusion, our investigation of the single-cell landscape of TIL, particularly focusing on the T and myeloid cell populations in MVIP primary HCC, underscores the critical roles of proliferative CD4$^+$ T cells and M2-like macrophages in shaping an immunosuppressive TME that is conducive to tumor progression. Identification of specific cellular communities and their interactions offers novel insights into the mechanistic underpinnings of HCC recurrence and progression in the context of MVI. The highlighted potential therapeutic targets, such as SPP1-CD44 and SPP1-IGTA4/ITGB1 interactions, pave the way for innovative approaches to counteract the immunosuppressive environment of HCC, enhance the efficacy of existing treatments and contributing to the development of new therapeutic strategies. Integrating single-cell analyses with functional studies and clinical trials will be crucial for advancing our understanding of HCC biology and improving outcomes for patients with this challenging disease.

Ethics approval

This study was reviewed and approved by the Ethics Committee of Chinese PLA General Hospital, with the approval number of S2022-313-02, dated July 27, 2022.

Consent for publication

All patients (or their proxies/legal guardians) provided written informed consent for the publication of their anonymized case details and images.

Data availability

The raw sequence data reported in this paper have been deposited in the Genome Sequence Archive (Genomics, Proteomics & Bioinformatics 2021) in National Genomics Data Center (Nucleic Acids Res 2022), China National Center for Bioinformation/Beijing Institute of Genomics, Chinese Academy of Sciences (GSA: HRA011337) that are publicly accessible at https://ngdc.cncb.ac.cn/gsa. Gene expression profiles, clinical information, and mutation data of HCC in this study are available from the public database (TCGA, https://portal.gdc.cancer.gov/).

The ICGC-LIHC data in the validation set were downloaded from the International Cancer Genome Consortium (ICGC, https://dcc.icgc. org/).

Funding

No funding

CRediT authorship contribution statement

Zhuoya Sun: Writing – original draft, Formal analysis, Data curation, Methodology, Software. **Biao Gao:** Formal analysis, Methodology, Software. **Lai Song:** Software. **Biying Wang:** Investigation. **Junfeng Li:** Investigation. **Hao Jiang:** Visualization, Investigation. **Xuerui Li:** Data curation. **Yang Yu:** Writing – review & editing. **Zishan Zhou:** Resources. **Zizhong Yang:** Visualization. **Xiaohui Sun:** Data curation. **Tianyu Jiao:** Data curation, Formal analysis. **Xiao Zhao:** Writing – review & editing, Project administration. **Shichun Lu:** Resources. **Shunchang Jiao:** Conceptualization, Supervision.

Declaration of competing interest

All authors disclosed no relevant relationships.

Acknowledgements

We would like to acknowledge the TCGA, ICGC and GEO for providing relevant data.

Appendix A. Supplementary data

Supplementary data to this article can be found online at https://doi.org/10.1016/j.heliyon.2024.e37233.

References

[1] J. Qi, M. Li, L. Wang, Y. Hu, W. Liu, Z. Long, Z. Zhou, P. Yin, M. Zhou, National and subnational trends in cancer burden in China, 2005–20: an analysis of national mortality surveillance data, Lancet Public Health 8 (2023) e943–e955, https://doi.org/10.1016/S2468-2667(23)00211-6.
[2] C. Lu, D. Rong, B. Zhang, W. Zheng, X. Wang, Z. Chen, W. Tang, Current perspectives on the immunosuppressive tumor microenvironment in hepatocellular carcinoma: challenges and opportunities, Mol. Cancer 18 (2019) 130, https://doi.org/10.1186/s12943-019-1047-6.
[3] I. El Hajra, M. Sanduzzi-Zamparelli, V. Sapena, S. Muñoz-Martínez, E. Mauro, N. Llarch, G. Iserte, A. Forner, J. Rios, J. Bruix, M. Reig, Outcome of patients with HCC and liver dysfunction under immunotherapy: a systematic review and meta-analysis, Hepatology 77 (2023) 1139–1149, https://doi.org/10.1097/HEP.0000000000000030.
[4] A. Beaufrère, S. Caruso, J. Calderaro, N. Poté, J.-C. Bijot, G. Couchy, F. Cauchy, V. Vilgrain, J. Zucman-Rossi, V. Paradis, Gene expression signature as a surrogate marker of microvascular invasion on routine hepatocellular carcinoma biopsies, J. Hepatol. 76 (2022) 343–352, https://doi.org/10.1016/j.jhep.2021.09.034.
[5] Z. Zheng, R. Guan, W. Jianxi, Z. Zhao, T. Peng, C. Liu, Y. Lin, Z. Jian, Microvascular invasion in hepatocellular carcinoma: a review of its definition, clinical significance, and comprehensive management, Journal of Oncology 2022 (2022) 1–10, https://doi.org/10.1155/2022/9567041.
[6] J. Li, F. Yang, J. Li, Z.-Y. Huang, Q. Cheng, E.-L. Zhang, Postoperative adjuvant therapy for hepatocellular carcinoma with microvascular invasion, World J. Gastrointest. Surg. 15 (2023) 19–31, https://doi.org/10.4240/wjgs.v15.i1.19.
[7] K. Li, R. Zhang, F. Wen, Y. Zhao, F. Meng, Q. Li, A. Hao, B. Yang, Z. Lu, Y. Cui, M. Zhou, Single-cell dissection of the multicellular ecosystem and molecular features underlying microvascular invasion in HCC, Hepatology (2023), https://doi.org/10.1097/HEP.0000000000000673.
[8] W. Gu, Z. Tong, Sorafenib in the treatment of patients with hepatocellular carcinoma (HCC) and microvascular infiltration: a systematic review and meta-analysis, J. Int. Med. Res. 48 (2020) 030006052094687, https://doi.org/10.1177/0300060520946872.
[9] V. Chew, L. Lai, L. Pan, C.J. Lim, J. Li, R. Ong, C. Chua, J.Y. Leong, K.H. Lim, H.C. Toh, S.Y. Lee, C.Y. Chan, B.K.P. Goh, A. Chung, P.K.H. Chow, S. Albani, Delineation of an immunosuppressive gradient in hepatocellular carcinoma using high-dimensional proteomic and transcriptomic analyses, Proc. Natl. Acad. Sci. U.S.A. 114 (2017), https://doi.org/10.1073/pnas.1706559114.
[10] M. Gryziak, K. Wozniak, L. Kraj, L. Rog, R. Stec, The immune landscape of hepatocellular carcinoma-where we are? Oncol. Lett. 24 (2022) 410, https://doi.org/10.3892/ol.2022.13530 (Review).
[11] L. Zheng, S. Qin, W. Si, A. Wang, B. Xing, R. Gao, X. Ren, L. Wang, X. Wu, J. Zhang, N. Wu, N. Zhang, H. Zheng, H. Ouyang, K. Chen, Z. Bu, X. Hu, J. Ji, Z. Zhang, Pan-cancer single-cell landscape of tumor-infiltrating T cells, Science 374 (2021) abe6474, https://doi.org/10.1126/science.abe6474.
[12] T. Wu, R. Fan, J. Bai, Z. Yang, Y.-S. Qian, L.-T. Du, C.-Y. Wang, Y.-C. Wang, G.-Q. Jiang, D. Zheng, X.-T. Fan, B. Zheng, J.-F. Liu, G.-H. Deng, F. Shen, H.-P. Hu, Y.-N. Ye, Q.-Z. Zhang, J. Zhang, Y.-H. Gao, J. Xia, H.-D. Yan, M.-F. Liang, Y.-L. Yu, F.-M. Sun, Y.-J. Gao, J. Sun, C.-X. Zhong, Y. Wang, H. Wang, F. Kong, J.-M. Chen, H. Wen, B.-M. Wu, C.-X. Wang, L. Wu, J.-L. Hou, X.-L. Liu, H.-Y. Wang, L. Chen, The development of a cSMART-based integrated model for hepatocellular carcinoma diagnosis, J. Hematol. Oncol. 16 (2023) 1, https://doi.org/10.1186/s13045-022-01396-z.
[13] J. Hu, L. Zhang, H. Xia, Y. Yan, X. Zhu, F. Sun, L. Sun, S. Li, D. Li, J. Wang, Y. Han, J. Zhang, D. Bian, H. Yu, Y. Chen, P. Fan, Q. Ma, G. Jiang, C. Wang, P. Zhang, Tumor microenvironment remodeling after neoadjuvant immunotherapy in non-small cell lung cancer revealed by single-cell RNA sequencing, Genome Med. 15 (2023) 14, https://doi.org/10.1186/s13073-023-01164-9.
[14] Y. Lu, A. Yang, C. Quan, Y. Pan, H. Zhang, Y. Li, C. Gao, H. Lu, X. Wang, P. Cao, H. Chen, S. Lu, G. Zhou, A single-cell atlas of the multicellular ecosystem of primary and metastatic hepatocellular carcinoma, Nat. Commun. 13 (2022) 4594, https://doi.org/10.1038/s41467-022-32283-3.
[15] D.H. Ballard, Microvascular invasion in hepatocellular carcinoma: bridging the global gap between imaging and clinical practice, Acad. Radiol. 30 (2023) 1528–1530, https://doi.org/10.1016/j.acra.2023.05.017.
[16] B. Isik, F. Gonultas, T. Sahin, S. Yilmaz, Microvascular venous invasion in hepatocellular carcinoma: why do recurrences occur? J. Gastrointest. Cancer 51 (2020) 1133–1136, https://doi.org/10.1007/s12029-020-00487-9.
[17] Z. Bai, Y. Zhou, Z. Ye, J. Xiong, H. Lan, F. Wang, Tumor-infiltrating lymphocytes in colorectal cancer: the fundamental indication and application on immunotherapy, Front. Immunol. 12 (2021) 808964, https://doi.org/10.3389/fimmu.2021.808964.
[18] S. Ahmadvand, Z. Faghih, M. Montazer, A. Safaei, M. Mokhtari, P. Jafari, A.-R. Talei, S. Tahmasebi, A. Ghaderi, Importance of CD45RO+ tumor-infiltrating lymphocytes in post-operative survival of breast cancer patients, Cell. Oncol. 42 (2019) 343–356, https://doi.org/10.1007/s13402-019-00430-6.
[19] E.J. Wherry, T cell exhaustion, Nat. Immunol. 12 (2011) 492–499, https://doi.org/10.1038/ni.2035.
[20] F. Mami-Chouaib, C. Blanc, S. Corgnac, S. Hans, I. Malenica, C. Granier, I. Tihy, E. Tartour, Resident memory T cells, critical components in tumor immunology, J. Immunotherapy Cancer 6 (2018) 87, https://doi.org/10.1186/s40425-018-0399-6.
[21] K. Sun, R. Xu, F. Ma, N. Yang, Y. Li, X. Sun, P. Jin, W. Kang, L. Jia, J. Xiong, H. Hu, Y. Tian, X. Lan, scRNA-seq of gastric tumor shows complex intercellular interaction with an alternative T cell exhaustion trajectory, Nat. Commun. 13 (2022) 4943, https://doi.org/10.1038/s41467-022-32627-z.
[22] Y. Wang, G.-Q. Zhu, R. Yang, C. Wang, W.-F. Qu, T.-H. Chu, Z. Tang, C. Yang, L. Yang, C.-W. Zhou, G.-Y. Miao, W.-R. Liu, Y.-H. Shi, M.-S. Zeng, Deciphering intratumoral heterogeneity of hepatocellular carcinoma with microvascular invasion with radiogenomic analysis, J. Transl. Med. 21 (2023) 734, https://doi.org/10.1186/s12967-023-04586-6.
[23] L. Dong, L. Peng, L. Ma, D. Liu, S. Zhang, S. Luo, J. Rao, H. Zhu, S. Yang, S. Xi, M. Chen, F. Xie, F. Li, W. Li, C. Ye, L. Lin, Y. Wang, X. Wang, D. Gao, H. Zhou, H. Yang, J. Wang, S. Zhu, X. Wang, Y. Cao, J. Zhou, J. Fan, K. Wu, Q. Gao, Heterogeneous immunogenomic features and distinct escape mechanisms in multifocal hepatocellular carcinoma, J. Hepatol. 72 (2020) 896–908, https://doi.org/10.1016/j.jhep.2019.12.014.

[24] J. Qi, H. Sun, Y. Zhang, Z. Wang, Z. Xun, Z. Li, X. Ding, R. Bao, L. Hong, W. Jia, F. Fang, H. Liu, L. Chen, J. Zhong, D. Zou, L. Liu, L. Han, F. Ginhoux, Y. Liu, Y. Ye, B. Su, Single-cell and spatial analysis reveal interaction of FAP+ fibroblasts and SPP1+ macrophages in colorectal cancer, Nat. Commun. 13 (2022) 1742, https://doi.org/10.1038/s41467-022-29366-6.

[25] J. Jiang, D.A. Diaz, S.P. Nuguru, A. Mittra, A. Manne, Stereotactic body radiation therapy (SBRT) plus immune checkpoint inhibitors (ICI) in hepatocellular carcinoma and cholangiocarcinoma, Cancers 15 (2022) 50, https://doi.org/10.3390/cancers15010050.

[26] T. Li, J. Guo, Y. Liu, Z. Du, Z. Guo, Y. Fan, L. Cheng, Y. Zhang, X. Gao, Y. Zhao, X. He, W. Wu, N. Gao, Y. Wu, J. Li, Y. Zhang, W. Kang, Z. Cai, W. Wang, X. Li, Y. Zan, M.H. Nguyen, F. Ji, Effectiveness and tolerability of camrelizumab combined with molecular targeted therapy for patients with unresectable or advanced HCC, Cancer Immunol. Immunother. 72 (2023) 2137–2149, https://doi.org/10.1007/s00262-023-03404-8.